

Hierarchical Conducting Polymer@Clay Core–Shell Arrays for Flexible All-Solid-State Supercapacitor Devices

Mingfei Shao, Zhenhua Li, Ruikang Zhang, Fanyu Ning, Min Wei,* David G. Evans, and Xue Duan

Electrochemical capacitors (ECs) or supercapacitors, storing energy by reversible ion adsorption or faradaic redox reactions on the surface of electrodes, are displaying important role in high performance power sources owing to their fast dynamic response, high energy delivery and excellent cycling lifespan in comparison with conventional batteries and capacitors.^[1] Such advantageous properties make them promising in a wide range of applications from portable/flexible electronics to hybrid vehicles, where high power density and long cycle-life are highly desirable. Various electrochemical active materials have been developed for ECs, including carbons,^[2] transition metal oxides/hydroxides^[3] and conducting polymers.^[4] However, for a given electrode material, high energy density, reversible charging/discharging, and long service time are practically hard to be achieved simultaneously as a consequence of some intrinsic limitations of individual constitution. For instance, carbon materials benefit from their good rate ability and high cyclical stability while suffer from low energy density (100–200 F g⁻¹) due to their inherent double layer capacitance properties.^[2c,5] In contrast, transition metal (Ni, Co, Mn, and Fe) hydroxides/oxides or conducting polymers possess high energy density but poor cycling stability.^[4a,6] Recently, concentrated efforts have been made to tackle this problem with constantly upgraded efficiency of ECs by developing advanced multifunctional nanocomposites^[7] or nanostructures.^[8] In spite of all these progresses, how to achieve an enhanced energy density and long endurance simultaneously by virtue of material exploration and fabrication strategy is still a huge challenge in ECs area.

Layered double hydroxides (LDHs) are a class of 2D structure anionic clays, which can be described by the general formula $[M^{II}_{1-x}M^{III}_x(OH)_2]^{z+}(A^{n-})_{z/n} \cdot yH_2O$ (M^{II} and M^{III} are divalent and trivalent metals respectively; A^{n-} is the interlayer anion compensating for the positive charge of

the brucite-like layers).^[9] Recently, transition metal-based LDHs materials have been reported as promising candidates for ECs owing to their low cost, high supercapacity, and environment-friendly nature.^[10] Unfortunately, LDHs-based ECs are hard to meet the ever-growing needs for the reversibility and power density as a result of poor conductivity. On the contrary, conducting polymers offer a desirable matrix toward fast electron transport in the faradic redox reaction, but suffer from cycling instability.^[4a,11] To solve this conundrum, hybridizing LDHs materials with conducting polymers, so as to improve the charge mobility and long-term stability, would be an effective route to obtain satisfactory overall electrochemical performance. In addition, a facile and efficient fabrication technique is highly necessary to achieve an elaborate nanostructure, in which all the electroactive species participates in faradaic redox reactions and a fast mass/electron transport is guaranteed.

Herein, we present the design and fabrication of a sophisticated nanoarray consisting of a conducting polymer (polypyrrole, PPy) core and LDHs shell via a two-step electrosynthesis method, and demonstrate its excellent behavior in high-performance flexible ECs. In view of this core–shell system (PPy@LDH), a synergistic effect plays a key role in achieving simultaneous high capacity and largely improved stability. The PPy core serves as a conductive and robust network to facilitate the electron collection and fast transport; while LDH shell acts as a protection layer to inhibit the volumetric swelling/shrinking of PPy during long-term charge/discharge cycling. Moreover, the potential electrochemically-active center in LDHs shell is excited extremely by virtue of the high conductivity of PPy core, which is normally concealed when LDHs material is used independently. The synergistic effect in this hierarchical core–shell nanostructure gives a decisive contribution to the promising overall performance of the all-solid-state asymmetric supercapacitor device: an energy density of ≈ 46 Wh kg⁻¹ (at 2.4 kW kg⁻¹), a power density of ≈ 12 kW kg⁻¹ (at 11.3 Wh kg⁻¹), and long life time (20 000 \times). It is worth mention that the cycling stability in this work, to the best of our knowledge, is superior to other reported flexible solid-state ECs. In addition, the fabrication route takes the advantages of easy manipulation, time, and cost effectiveness, which would guarantee a large-scale manufacture for practical applications in energy storage devices.

Dr. M. Shao, Z. Li, R. Zhang, F. Ning, Prof. M. Wei,
Prof. D. G. Evans, Prof. X. Duan
State Key Laboratory of Chemical Resource Engineering
Beijing University of Chemical Technology
Beijing 100029, China
E-mail: weimin@mail.buct.edu.cn



DOI: 10.1002/sml.201403421

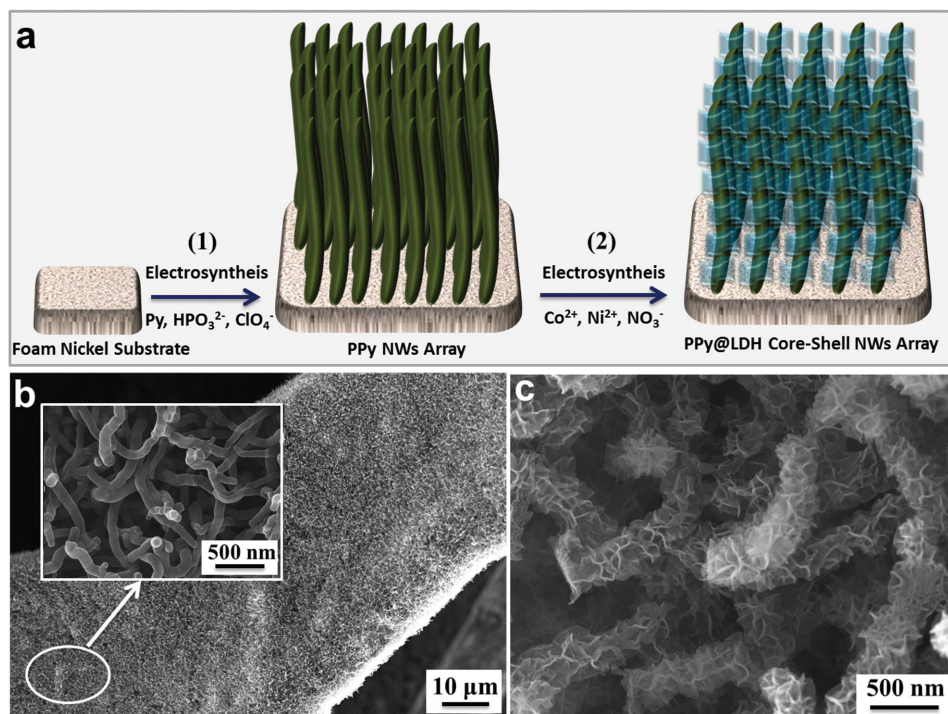


Figure 1. a) A schematic illustration for the fabrication of PPY@LDH core-shell NWs array; SEM images of b) PPY NWs and c) PPY@LDH core-shell NWs array on foam nickel substrate.

PPY@LDH core-shell arrays are synthesized on the surface of foam nickel substrate via a two-step procedure (**Figure 1a**): electrochemical polymerization of PPY nanowires (NWs) followed by electrochemical synthesis of LDH on the surface of as-obtained PPY NWs. As shown in **Figure 1b**, numerous wormlike PPY NWs are produced on the foam nickel substrate with a uniform diameter in the range 80–100 nm and length distribution of 2–3 μm . The electrochemical polymerization process of PPY NWs was further studied by control of the reaction time. Some small PPY dots (≈ 15 nm) appear on the surface of substrate at the initial 50 s (**Figure S1a**, Supporting Information). As the reaction time increases from 50 to 500 s, PPY NWs are observed with gradually-enhanced density and obviously-changed dimensionalities (diameter from ≈ 40 to ≈ 110 nm; length from ≈ 200 nm to ≈ 3 μm), and finally become predominant and even overlays the whole substrate (**Figure S1b–d**, Supporting Information). After coating with LDH nanoflakes (≈ 65 nm in width and ≈ 8 nm in thickness) by a subsequent electrochemical route (see Experimental Section for synthesis details), core-shell PPY@CoNi-LDH nanoarrays with uniform size, and morphology are obtained, with intercrossing LDH nanoplatelets perpendicularly grafted to the polymer core (**Figure 1c**). It is found that the electrochemical synthesis time (0–200 s) of LDH shell imposes a significant influence on the shell thickness and morphology (**Figure S2**, Supporting Information); a prolonged time leads to a much thicker and denser LDH shell. The core-shell nanostructure was further confirmed by transmission electron microscopy (TEM, **Figure 2a**), from which the core diameter of ≈ 91 nm and shell thickness of ≈ 56 nm were identified clearly. The d -spacing from high resolution

TEM (HRTEM) is ≈ 0.25 nm, corresponding to the LDH (012) plane, as indicated by the lattice fringes (**Figure 2b**), which is consistent with the further X-ray diffraction (XRD) result. **Figure 2c** shows the XRD patterns of PPY and PPY@LDH, respectively. The broad peak at 2θ 20° – 30° presents a reflection characteristic of amorphous PPY NWs. After coating with the LDH layer, the (003), (006), (012), and (110) reflection of a typical LDH material are clearly observed, indicating the high crystallinity of LDH shell. Although XRD pattern shows that the (003) is probably the richest diffraction plane, the HRTEM electron beam is perpendicular to the (003) lattice plane of LDH nanoflakes with a strong probability, resulting in the absence of (003) interplanar distance in the HRTEM image. This is consistent with the Weiss zone law.

The chemical composition and structure of PPY@LDH core-shell NWs array were further determined by X-ray spectroscopy (EDX) analysis, Raman spectra, FT-IR, and XPS technique. The EDX spectrum verifies the uniform presence of C, O, P, and Ni (from foam nickel substrate) for the pure PPY NWs sample (**Figure 2d**). The appearance of element Co and the signal enhancement of element Ni for the PPY@LDH NWs array demonstrate the successful introduction of CoNi-LDH shell. Raman spectrum of PPY@LDH (**Figure 2e**) displays peaks at 1559 and 1330 cm^{-1} , corresponding to the π -conjugated structure and ring stretching mode of PPY backbone, respectively;^[12] the new peak at 523 cm^{-1} is attributed to the stretching of OH–O bonds between carbonate ions and water molecules in the interlayer of CoNi-LDH. The FT-IR technique was also used to identify the nature/symmetry of PPY and chemical composition

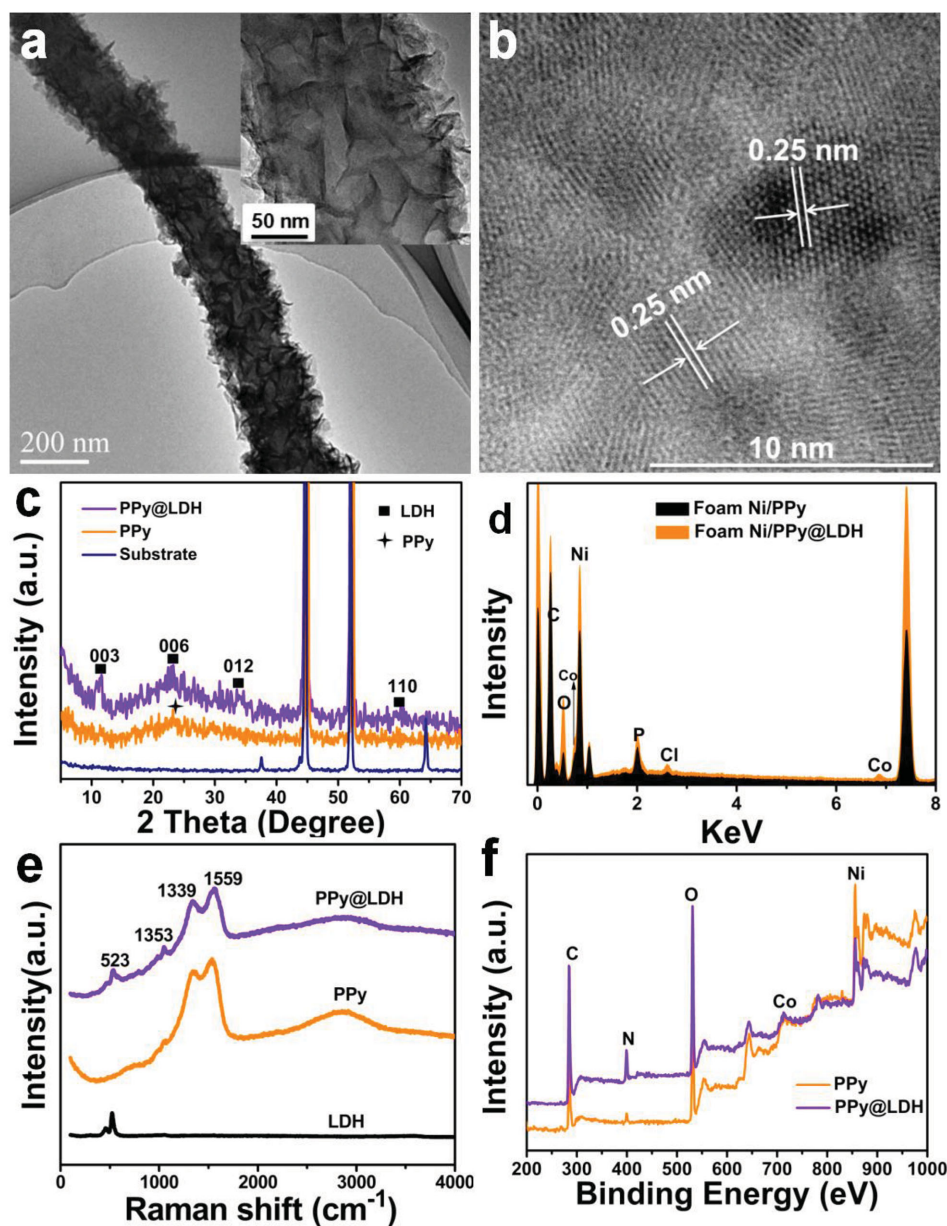


Figure 2. a) TEM and b) HRTEM image for the PPy@LDH NWs array; c) XRD; d) EDX; e) Raman; and f) XPS spectra for the pristine PPy and PPy@LDH NWs array, respectively.

of LDH (Figure S3, Supporting Information). The bands at 1643 and 1413 cm^{-1} are due to the fundamental stretching vibrations of pyrrole rings; bands at 1413 and 1100 cm^{-1} are ascribed to the C–N stretching and C–H deformation vibration, respectively. After coating with LDH, a new band at 1468 cm^{-1} is observed, which is assigned to mode ν_3 of inter-layer carbonate species. Surface elemental analysis was carried out by XPS over the PPy and PPy@LDH sample. The full XPS spectrum of PPy@LDH NWs array reveals signals of Co, Ni, O, N, and C element; while Co $2p$ peak is absent in pristine PPy array (Figure 2f). The binding energy of Co $2p_{3/2}$ peak shows a complex structure broadened by multiplet splitting effects (Figure S4a, Supporting Information), which can be decomposed to 782.3 and 780.1 eV. This indicates the presence of both Co^{2+} and Co^{3+} oxidation state in the PPy@

LDH sample. Figure S4b (Supporting Information) shows the binding energy of Ni $2p$ at 855.3 eV, corresponding to the Ni(II) oxidation state.

Figure 3a shows the cyclic voltammograms (CVs) of pristine PPy, CoNi-LDH, and PPy@CoNi-LDH with different LDH deposition time (50, 100, 150, and 200 s) in 1 M KOH solution at a scan rate of 1 mV s^{-1} . For the PPy NWs array, the redox couple (P1 and P2) are due to the faradaic redox reaction of PPy via doping/dedoping in alkaline solution.^[4a] Compared with the CV curves of $\text{Co}(\text{OH})_2$ and $\text{Ni}(\text{OH})_2$ electrode (Figure S4, Supporting Information), the CoNi-LDH electrode (SEM image: Figure S5, Supporting Information) consists of two pairs of redox peaks: the first redox couple (P3 and P4) are due to the $\text{Co}^{2+}/\text{Co}^{3+}$ reaction; while the second redox couple (P5 and P6) are attributed to the

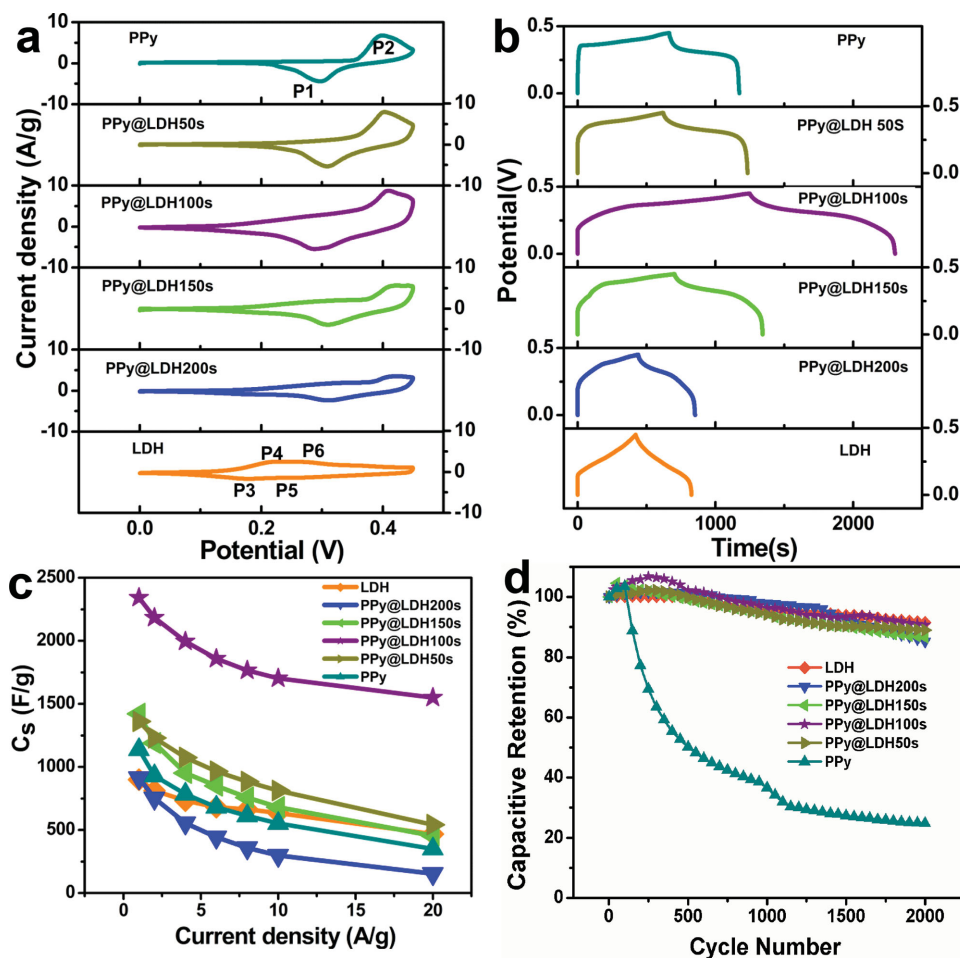


Figure 3. a) CVs curves and b) GV charge/discharge curves for the pristine PPy, LDH, and PPy@LDH samples (LDH deposition time: 50, 100, 150, and 200 s); c) current density dependence of specific capacitance; and d) cycling performance for the pristine PPy, LDH, and PPy@LDH samples (LDH deposition time: 50, 100, 150, and 200 s, respectively).

$\text{Ni}^{2+}/\text{Ni}^{3+}$ conversion. In the case of PPy@CoNi-LDH samples, the area of CV curve for the hybrid electrode increases along with the deposition of LDH shell on PPy NWs core and reaches a maximum for the PPy@LDH sample (100 s), indicating a largely enhanced capacitance. However, the capacitance decreases significantly with further elongation of the deposition time, which demonstrates that an excess of LDH incorporation leads to a depressed electrochemical activity. It is known that a large specific surface area and suitable mesopore distribution of supercapacitance materials are key factors to endow fast mass transportation and redox reaction. An over-dense packing of LDH shell on PPy core gives less exposure of active sites, which thereby diminishes the faradic reactions and hinders the charge transfer. Figure 3b shows the galvanostatic (GV) charge/discharge characteristics of various PPy@LDH NWs arrays within a potential range from 0 to 0.5 V, in which the nonlinear charge/discharge curves verify the pseudo-capacitance nature. The weight of these PPy@CoNi-LDH electrodes with various deposition time of CoNi-LDH shell is listed in Table S1 (Supporting Information). The corresponding specific capacitance are 1137, 897, 1360, 2342, 1421, and 913 F g^{-1} at a current density of 1 A g^{-1} for the PPy, LDH, PPy@LDH (50, 100, 150, and

200 s), respectively, further demonstrating the highest specific capacitance for the PPy@LDH (100 s) sample.

Rate capability is a key factor for evaluating the power applications of supercapacitors, which was determined by using the CV at varied scan rates (Figure S7, Supporting Information) and GV technique at different charge/discharge current densities (Figure S8, Supporting Information). The specific capacitances of the six samples derived from the discharging curves at various charge/discharge current densities are shown in Figure 3c. Within the whole current density range, the PPy@LDH (100 s) yields substantially higher specific capacitance than that of the other samples, in line with the CV and GV results. At a high current density of 20 A g^{-1} , the specific capacitance maintains only 30.9% and 51.9% for the pristine PPy NWs array and LDH sample, respectively. In the case of PPy@LDH (100 s) sample however, 66.2% of the capacitance is still retained, much superior to the other five control samples. Cycling capability or cycling life is an important requirement for supercapacitor applications, which largely restricts the energy storage performance of ECs. The cycling life tests over PPy@LDH-based electrodes for 2000 cycles at a current density of 10 A g^{-1} were carried out using GV charge/discharge technique in the potential window

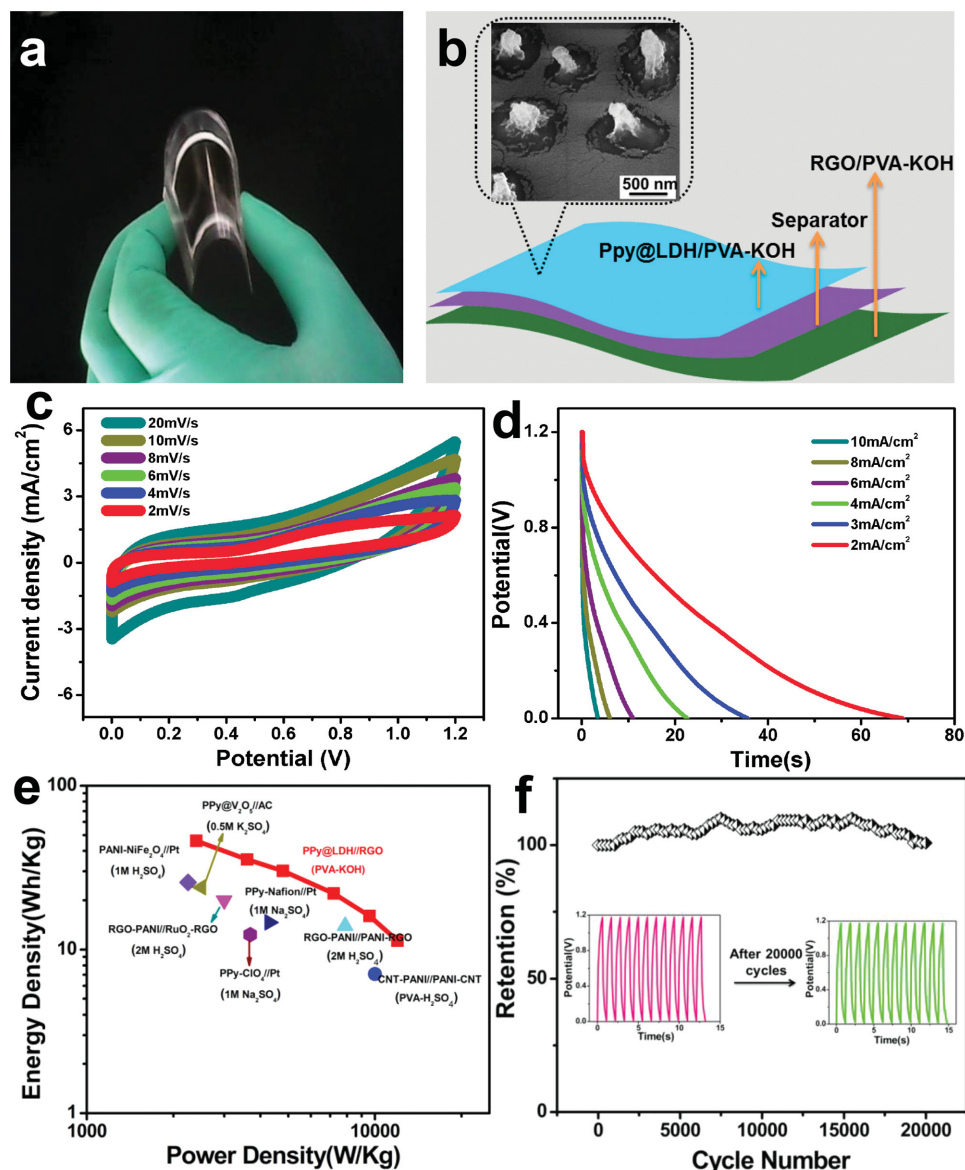


Figure 4. a) A photograph of the flexible PPy@LDH-based all-solid-state EC device; b) schematic representation of the flexible asymmetric EC device based on PPy@LDH, RGO electrode, and PVA/KOH electrolyte; c) CV curves of the device at various scan rates; d) GV charge–discharge curves of the device at various current densities; e) Ragone plots of the flexible EC device, in comparison with reference samples; f) cycling performance of the device at a current density of 20 A g⁻¹ (inset: GV results of the first and last 12 cycles).

0–0.5 V (Figure 3d). The pristine PPy NWs array shows the worst cycling stability (24.7% retention), in-line with the previously reported results (normally less than 50% for most PPy-based electrodes after 1000 cycles).^[4] The poor stability is ascribed to the intrinsic volumetric alternation of PPy during the charge/discharge process, resulting in the structural breakdown and fast capacitance decay. Inspiringly in this work, after introducing LDH shell, a largely enhanced cycling stability is obtained: the PPy@LDH (100 s) sample gives maximum capacitance retention of 90.7%. The results further verify the great potentiality of PPy@LDH nanocomposite as efficient supercapacitor material with high specific capacitance and good cycling stability.

Lightweight and flexible solid-state ECs have attracted considerable attention along with the increasing power and

energy demands for portable electronics. Here, flexible solid-state asymmetric ECs were fabricated by using foam Ni supported PPy@LDH NWs as the positive electrode, a reduced graphene oxide (RGO) film as the negative electrode and poly(vinyl alcohol) (PVA)/KOH as the solid electrolyte. The area of all the fabricated solid-state ECs is 1.0 cm² and the weight of the whole cell is ≈50 mg. As shown in **Figure 4a**, the obtained device gives excellent flexibility without any cracks upon bending. The configuration of all-solid-state flexible EC device described herein is schematically shown in **Figure 4b**. The surface morphology of positive electrode (**Figure 4b**, inset) reveals that the PPy@LDH NWs are surrounded by the PVA/KOH solid electrolyte, which guarantees necessary medium conditions toward redox reactions. **Figure 4c** displays the CV curves of the asymmetric EC measured at the scan rate

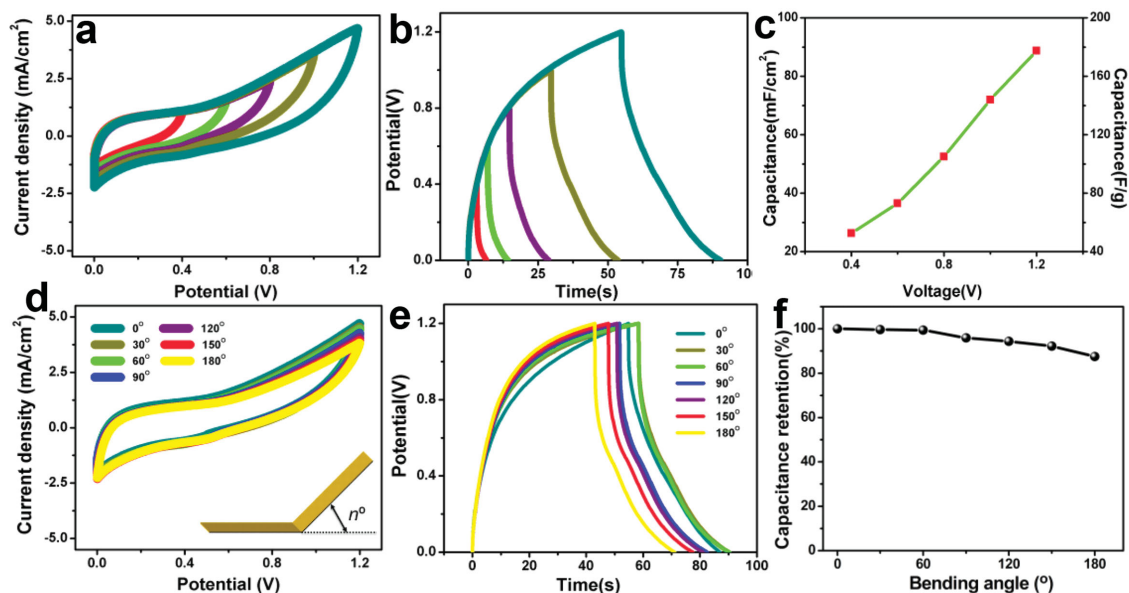


Figure 5. a) CV curves; b) GV charge/discharge curves; c) volumetric and specific capacitance of the asymmetric supercapacitor with the increase of potential window. d) CV curves; e) GV charge/discharge curves; and f) capacitance retention of the flexible EC device bending at different angles.

ranging in $2\text{--}20\text{ mV s}^{-1}$ between 0 and 1.2 V. Different from the three-electrode electrochemical feature of PPy@LDH electrode, the obtained all-solid-state device exhibits a quasi-rectangular CV geometry as electric double layer capacitors (EDLC), indicating a capacitive behavior. The energy (E) and power (P) density are calculated from GV discharge curves (Figure 4d) and plotted on the Ragone diagram (Figure 4e). The maximum energy density of 46 Wh kg^{-1} (at a power density of 2.4 kW kg^{-1}) and power density of 12 kW kg^{-1} (at an energy density of 11.3 Wh kg^{-1}) are achieved at an operating voltage of 1.2 V, superior to previously reported systems such as pure CPs,^[13] CPs-metal oxides,^[14] and CPs-carbon materials composites.^[15] Furthermore, Figure 4f displays the long-term cycle stability by GV charge/discharge at a current density of 20 mA cm^{-2} , from which it is interesting to find the capacitance of the PPy@LDH-based device even increases $\approx 15.4\%$ after cycling 20 000 times. The enhancement in specific capacitance can be attributed to the gradual activation of redox species exposed to the solid electrolyte upon repetitive charge/discharge cycling (self-activation process), which has also been reported previously.^[16] Compared with the reported CoNi-LDH or corresponding spinel electrodes (Table S2, Supporting Information),^[17] the PPy@CoNi-LDH NWs array supercapacitor device in this work demonstrates a comparable energy output, with advantage in energy density at high power densities. In particular, the stability of PPy@CoNi-LDH NWs-based device is extremely enhanced: 115.4% capacitance retention is obtained after 20 000 cycles; while less than 93% was reported after 5 000 cycles for the reference samples.

From the viewpoint of practical applications, soft and portable electronics may require highly flexible power sources working at various operation voltages and powers. **Figure 5a** shows a series of CV measurements of the asymmetric EC devices with different cell voltages varying from 0.0–0.4 V to 0.0–1.2 V. It is observed that Faradic

reaction (the larger peak current) occurs more sufficiently with the increase of operating potential to 1.2 V. Moreover, the charge/discharge curves of the PPy@LDH EC device at a current density of 20 mA cm^{-2} remain nearly symmetric at an operating potential as high as 1.2 V (Figure 5b), suggesting that the device exhibits ideal capacitive characteristics with a rapid $I\text{--}V$ response and small equivalent series resistance.^[18] Figure 5c displays a variation of the volumetric and specific capacitance of the asymmetric supercapacitor with an increasing potential window. The volumetric capacitance enhances significantly from 26.3 to 88.7 mF cm^{-2} as the operating potential increases from 0–0.4 to 0–1.2 V (for detailed calculations, see Experimental Section). The effect of curvature on the device performance was examined by testing CV curves and charge/discharge behavior at seven different bending angles (from 0° to 180°). As shown in Figure 5d, no apparent change in the CV curves is observed; furthermore, $\approx 87.5\%$ capacitance is maintained with a bending angle of 180° based on the discharge curves (Figure 5e), revealing a satisfactory electrochemical performance of the EC even under the bending conditions.

As demonstrated in the electrochemical results (Figure 3), the specific capacitance of the PPy@LDH core-shell NWs array (2342 F g^{-1} ; current density 1 A g^{-1}) is 2.1, 2.6, and 1.2 times higher than that of pristine PPy (1137 F g^{-1}), LDH (897 F g^{-1}), and the summation of these two constitutes (2034 F g^{-1}), respectively. The specific capacitance enhancement of PPy@LDH is attributed to the synergetic effect of PPy core and LDH shell. On one hand, the PPy core provides pseudocapacitance and guarantees excellent electrical conductivity at the same time. The Nyquist plots of the electrochemical impedance spectroscopy (EIS) spectra for pristine PPy, LDH and PPy@LDH (50, 100, 150, and 200 s) were measured respectively to understand the enhanced

conductivity (Figure S9, Supporting Information). The semicircle-like shape of EIS spectra for these samples is observed with the sequence order of R_{ct} : PPy@LDH (100 s) < PPy@LDH (50 s) < PPy ≤ PPy@LDH (150 s) < PPy@LDH (200 s) ≤ LDH. The results clearly demonstrate that the PPy@LDH (100 s) sample possesses the lowest resistance and thus allows for the fastest electron transfer. On the other hand, the large improvement in the conductivity stimulates the potential electrochemically-active unit of LDH shell, which is concealed by the poor carrier mobility of individual LDH material, giving rise to greatly enhanced energy and power output as well as a better rate capability for the PPy@LDH-based EC device.

In addition to the capacitance and rate capability, the cycling stability of the PPy@LDH device is extremely enhanced as well. The synergetic effect further reflects in the fact that LDH not only provides abundant redox active sites but also acts as an effective protection layer to keep PPy NWs from structural breakdown upon charge/discharge process. As shown in Figure S10 (Supporting Information), after 2000 cycles, the surface of pristine PPy electrode was seriously destroyed owing to the facile volumetric swelling/shrinking during charge/discharge cycling, whereas the PPy NWs array coated by LDH shell remain its original hierarchical architecture. This indicates that the LDH shell effectively restrains the structural variation of PPy NWs core during electrochemical reactions. Consequently, the PPy@LDH-based device gives a surprisingly high cycling stability: the capacitance increases ≈15.4% after cycling 20 000 times, which is the best value reported for the flexible pseudo-ECs to the best of our knowledge. The high energy and power density output along with the excellent cycling stability of the obtained PPy@LDH-based all-solid-state EC device meet the requirements of both high energy density and long endurance simultaneously, which are prerequisites for practical energy storage devices. In addition, the preparation of PPy@LDH NWs array electrode is time and cost effective, which can serve as a general strategy for the scalable manufacture of electrode materials for energy storage and conversion.

In summary, the hierarchical PPy@LDH core-shell array has been successfully obtained via a facile and effective two-step electrosynthesis method. In this integrated configuration, the PPy core guarantees an excellent conductivity while the LDH shell acts as a protection layer to enhance the structural stability. Being electrochemically active species, both PPy and LDH offer improved pseudocapacitance performance, as a result of the enhanced overall conductivity in this system. By virtue of the synergistic effect between PPy core and LDH shell, the as-fabricated asymmetrical, flexible all-solid-state EC device (PPy@LDH/RGO) exhibits a high energy density (46 Wh kg⁻¹ at a power density of 2.4 kW kg⁻¹) and excellent cycling stability (15.4% increase in capacitance after cycling for 20 000 times). It is expected the CPs@LDH-based device can be potentially used in highly efficient and stable energy storage.

Experimental Section

Preparation of PPy NWs Array: The PPy nanowire array was prepared using a facile electrochemical polymerization method.^[19]

Typically, nickel foam (10 × 40 × 0.1 mm) was pretreated with 2 M HCl solution, absolute ethanol, acetone, and deionized water (each for 15 min), to ensure a clean surface. Electrochemical polymerization was carried out in a three electrode system, with the nickel foam as working electrode, Pt wire as counter electrode and a saturated calomel electrode (SCE) as reference electrode, in aqueous electrolyte containing 0.15 M pyrrole, 0.2 M Na₂HPO₄, and 0.001 M NaClO₄ by potentiostatic deposition at a potential of 0.9 V versus SCE. A uniform black film was obtained.

Synthesis of the PPy@CoNi-LDH Core-Shell NWs Array: The PPy@CoNi-LDH core-shell NWs array was prepared using a facile electrosynthesis method. The obtained PPy NWs array was used as the working electrode and placed in an electrochemical cell in a three-electrode configuration, by using Pt wire as counter electrode and a saturated calomel electrode (SCE) as the reference electrode. The electrolyte for electrodeposition of CoNi-LDH was obtained by dissolving CoCl₂·6H₂O (1.784 g) and Ni(NO₃)₂·6H₂O (2.181 g) in 50 mL of distilled water. The potentiostatic deposition was carried out at a potential of -1.0 V versus SCE. The electrochemical synthesis of CoNi-LDH was achieved by the reduction of NO₃⁻ occurring on the working electrode (NO₃⁻ + H₂O + 2e⁻ → NO₂⁻ + 2OH⁻), in which the resulting OH⁻ leads to the coprecipitation of CoNi-LDH on the surface of polypyrrole (PPy) conducting substrate. The whole electrosynthesis process can be accomplished within hundreds of seconds at the room temperature. The resulting PPy@LDH NWs array was withdrawn and rinsed with distilled water.

Preparation of the Solid Electrolyte: Polyvinyl alcohol (PVA) (molecular weight: 75000–80000) and KOH were used as received. The PVA-KOH solid electrolyte was prepared as follows: PVA (3.0 g) and KOH (3.0 g) were dissolved in 30 mL water with vigorous and continuous stirring for 5 h at 85 °C, until a complete dissolution and formation of a jelly-like solution. The resulting gel was heated at 60 °C in a vacuum oven to evaporate excess water. The resulting PVA/KOH polymer film was stored in a polyethylene bag before use.

Fabrication of the RGO Electrode: A modified Hummers method was utilized to synthesize the powdered oxidized graphite.^[20] The obtained GO (specific surface area: 122.5 m² g⁻¹; C/O molar ratio: 3.23; particle size: 1.5–3 μm in lateral length and 0.84 nm in thickness (shown in Figure S11a, Supporting Information)) was dispersed in deionized water to yield a yellow-brown suspension (5 mg mL⁻¹), followed by vacuum filtration through foam Ni and a polyamide membrane filter (220 nm pore size, Shanghai Xinya) for 6 h. The Ni foam was then withdrawn (the color was brown) and immersed into a NaBH₄ aqueous solution (1 g mL⁻¹) for 0.5 h to endow the reduction of GO (denoted as RGO). The obtained black Ni foam/RGO (Figure S11b, Supporting Information) was used as the counter electrode for the all-solid-state EC device.

Fabrication of PPy@CoNi-LDH/RGO SC Device: The PPy@CoNi-LDH/RGO EC device (area: 1 cm × 1 cm) was fabricated by assembly of a PVA-KOH solid electrolyte membrane between the PPy@CoNi-LDH/Ni and the RGO/Ni electrode face-to-face. After hot pressing at 60 °C for 5 min, the electrolyte was solidified to produce a sandwich structure. The overall thickness of this all-solid-state EC is ≈0.3 mm, facilitating a close contact between the electrolyte and electrode.

Characterization: X-ray diffraction patterns of the core-shell NWs array samples were collected on a Shimadzu XRD-6000

diffractometer using a Cu K α source, with a scan step of 0.02° and a scan range between 3° and 70°. FTIR spectra were recorded on a NICOLET NEXUS470 Fourier transform-infrared spectrometer. X-ray photoelectron spectra (XPS) were recorded on a Thermo VG ESCALAB 250 X-ray photoelectron spectrometer at a pressure of about 2×10^{-9} Pa using Al K α X-rays as the excitation source. The morphology of the core-shell NWs array was investigated using a scanning electron microscope (SEM; Zeiss SUPRA 55) with an accelerating voltage of 20 kV, combined with energy dispersive X-ray spectroscopy (EDX) for the determination of metal composition. Transmission electron microscopy (TEM) images were recorded with Philips Tecnai 20 and JEOL JEM-2010 high-resolution transmission electron microscopes. The accelerating voltage was 200 kV in each case.

Electrochemical Performance Measurements: Electrodes were tested on a CHI 660E electrochemical workstation (Shanghai Chenhua Instrument Co., China) in a three-electrode electrochemical cell using a 1 M KOH aqueous solution as electrolyte at room temperature. The NWs array on Ni foam was directly used as the working electrode. A Pt wire and a SCE were used as the counter and reference electrode, respectively. The distance between the working electrode and the counter electrode was 2 cm.

The specific capacitance of the PPy@LDH samples was calculated from the charge-discharge curves based on the following equation:

$$C = \frac{I \times \Delta t}{m \times \Delta V} \quad (1)$$

where C (F g $^{-1}$) is the specific capacitance; I (A) refers to the discharge current; ΔV (V) represents the potential change within the discharge time Δt (s), and m (g) corresponds to the total weight of the PPy@LDH NWs array.

Energy density and power density of the flexible EC device were calculated using the following equations:

$$C = \frac{I \times \Delta t}{m \times \Delta V} \quad (2)$$

$$E = \frac{C \times \Delta V^2}{2} \quad (3)$$

$$P = \frac{E}{\Delta t} \quad (4)$$

where C (F g $^{-1}$) is the capacitance of EC device; I (A) represents the discharge current; ΔV (V) refers to the potential change within the discharge time Δt (s); m (g) is the total weight of EC device; E (Wh kg $^{-1}$); and P (kW kg $^{-1}$) correspond to the energy density and power density, respectively.

Supporting Information

Supporting Information is available from the Wiley Online Library or from the author.

Acknowledgements

This work was supported by the National Natural Science Foundation of China (NSFC), the Fundamental Research Funds for the Central Universities (YS1406), the 973 Program (Grant No. 2014CB932102), the Beijing Natural Science Foundation (Grant No. 2132043). M. Wei particularly appreciates the financial aid from the China National Funds for Distinguished Young Scientists of the NSFC.

- [1] a) P. Simon, Y. Gogotsi, *Nat. Mater.* **2008**, *7*, 845; b) Z. S. Wu, K. Parvez, X. Feng, K. Mullen, *Nat. Commun.* **2013**, *4*, 2487; c) R. Sharma, C. C. B. Bufon, D. Grimm, R. Sommer, A. Wollatz, J. Schadowald, D. J. Thurmer, P. F. Siles, M. Bauer, O. G. Schmidt, *Adv. Energy Mater.* **2014**, *4*, 1301631; d) X. Lang, A. Hirata, T. Fujita, M. Chen, *Nat. Nanotechnol.* **2011**, *6*, 232; e) J. R. Miller, P. Simon, *Science* **2008**, *321*, 651; f) Y. Zhu, S. Murali, M. D. Stoller, K. J. Ganesh, W. Cai, P. J. Ferreira, A. Pirkle, R. M. Wallace, K. A. Cychoz, M. S. D. Thommes, E. A. Stach, R. S. Ruoff, *Science* **2011**, *332*, 1537; g) X. Peng, L. Peng, C. Wu, Y. Xie, *Chem. Soc. Rev.* **2014**, *43*, 3303.
- [2] a) Z. Niu, W. Zhou, J. Chen, G. Feng, H. Li, W. Ma, J. Li, H. Dong, Y. Ren, D. Zhao, S. Xie, *Energy Environ. Sci.* **2011**, *4*, 1440; b) D. H. Seo, Z. J. Han, S. Kumar, K. Ostrikov, *Adv. Energy Mater.* **2013**, *3*, 1316; c) Q. Meng, H. Wu, Y. Meng, K. Xie, Z. Wei, Z. Guo, *Adv. Mater.* **2014**, *26*, 4100; d) L. Dai, D. W. Chang, J. B. Baek, W. Lu, *Small* **2012**, *8*, 1130.
- [3] a) J. Bae, M. K. Song, Y. J. Park, J. M. Kim, M. Liu, Z. L. Wang, *Angew. Chem. Int. Ed.* **2011**, *50*, 1683; b) H. L. Wang, H. S. Casalongue, Y. L. Liang, H. J. Dai, *J. Am. Chem. Soc.* **2010**, *132*, 7472; c) X. Xia, J. Tu, Y. Zhang, X. Wang, C. Gu, X. Zhao, H. Fan, *ACS Nano* **2012**, *6*, 5531; d) J. Kang, L. Chen, Y. Hou, C. Li, T. Fujita, X. Lang, A. Hirata, M. Chen, *Adv. Energy Mater.* **2013**, *3*, 857.
- [4] a) J. Zang, S. J. Bao, C. M. Li, H. Bian, X. Cui, Q. Bao, C. Q. Sun, J. Guo, K. Lian, *J. Phys. Chem. C* **2008**, *112*, 14843; b) T. Liu, L. Finn, M. Yu, H. Wang, T. Zhai, X. Lu, Y. Tong, Y. Li, *Nano Lett.* **2014**, *14*, 2522.
- [5] L. L. Zhang, X. S. Zhao, *Chem. Soc. Rev.* **2009**, *38*, 2520.
- [6] G. P. Wang, L. Zhang, J. J. Zhang, *Chem. Soc. Rev.* **2012**, *41*, 797.
- [7] a) L. Yuan, B. Yao, B. Hu, K. Huo, W. Chen, J. Zhou, *Energy Environ. Sci.* **2013**, *6*, 470; b) Z. S. Wu, K. Parvez, A. Winter, H. Viekler, X. Liu, S. Han, A. Turchanin, X. Feng, K. Müllen, *Adv. Mater.* **2014**, *26*, 4552; c) G. Yu, L. Hu, M. Vosgueritchian, H. Wang, X. Xie, J. R. McDonough, X. Cui, Y. Cui, Z. Bao, *Nano Lett.* **2011**, *11*, 2905.
- [8] a) X. Lu, T. Zhai, X. Zhang, Y. Shen, L. Yuan, B. Hu, L. Gong, J. Chen, Y. Gao, J. Zhou, Y. Tong, Z. L. Wang, *Adv. Mater.* **2012**, *24*, 938; b) C. Zhou, Y. Zhang, Y. Li, J. Liu, *Nano Lett.* **2013**, *13*, 2078; c) D. W. Wang, F. Li, M. Liu, G. Q. Lu, H. M. Cheng, *Angew. Chem. Int. Ed.* **2008**, *47*, 373; d) Y. Zhao, J. Liu, Y. Hu, H. Cheng, C. Hu, C. Jiang, L. Jiang, A. Cao, L. Qu, *Adv. Mater.* **2013**, *25*, 591.
- [9] A. I. Khan, D. O'Hare, *J. Mater. Chem.* **2002**, *12*, 3191.
- [10] a) V. Gupta, S. Gupta, N. Miura, *J. Power Sources* **2008**, *175*, 680; b) M. F. Shao, F. Y. Ning, Y. F. Zhao, J. W. Zhao, M. Wei, D. G. Evans, X. Duan, *Chem. Mater.* **2012**, *24*, 1192; c) Z. Gao, J. Wang, Z. Li, W. Yang, B. Wang, M. Hou, Y. He, Q. Liu, T. Mann, P. Yang, M. Zhang, L. Liu, *Chem. Mater.* **2011**, *23*, 3509; d) J. W. Zhao, J. L. Chen, S. M. Xu, M. F. Shao, Q. Zhang, F. Wei, J. Ma, M. Wei, D. G. Evans, X. Duan, *Adv. Funct. Mater.* **2014**, *24*, 2938; e) J. Han, Y. Dou, J. Zhao, M. Wei, D. G. Evans, X. Duan, *Small* **2013**, *9*, 98; f) R. Ma, X. Liu, J. Liang, Y. Bando, T. Sasaki, *Adv. Mater.* **2014**, *26*, 4173.
- [11] G. A. Snook, P. Kao, A. S. Best, *J. Power Sources* **2011**, *196*, 1.

- [12] W. Zhang, X. Wen, S. Yang, *Langmuir* **2003**, *19*, 4420.
- [13] C. Meng, C. Liu, L. Chen, C. Hu, S. Fan, *Nano Lett.* **2010**, *10*, 4025.
- [14] a) B. Senthilkumar, K. V. Sankar, C. Sanjeeviraja, R. K. Selvan, *J. Alloys Compd.* **2013**, *553*, 350; b) Q. Qu, Y. Zhu, X. Gao, Y. Wu, *Adv. Energy Mater.* **2012**, *2*, 950.
- [15] a) J. Zhang, J. Jiang, H. Li, X. S. Zhao, *Energy Environ. Sci.* **2011**, *4*, 4009; b) V. Gupta, N. Miura, *Electrochim. Acta* **2006**, *52*, 1721; c) P. Yu, X. Zhao, Z. Huang, Y. Li, Q. Zhang, *J. Mater. Chem. A* **2014**, *2*, 14413.
- [16] a) X. Lu, D. Zheng, T. Zhai, Z. Liu, Y. Huang, S. Xie, Y. Tong, *Energy Environ. Sci.* **2011**, *4*, 2915; b) L. Yuan, B. Yao, B. Hu, K. Huo, W. Chen, J. Zhou, *Energy Environ. Sci.* **2013**, *6*, 470; c) Z. Gao, J. Wang, Z. Li, W. Yang, B. Wang, M. Hou, Y. He, Q. Liu, T. Mann, P. Yang, M. Zhang, L. Liu, *Chem. Mater.* **2011**, *23*, 3509.
- [17] a) V. Gupta, S. Gupta, N. Miura, *J. Power Sources* **2008**, *175*, 680; b) X. Wang, A. Sumboja, M. Lin, J. Yan, P. S. Lee, *Nanoscale* **2012**, *4*, 7266; c) L. Huang, D. Chen, Y. Ding, S. Feng, Z. L. Wang, M. Liu, *Nano Lett.* **2013**, *13*, 3135; d) K. Xu, X. Huang, Q. Liu, R. Zou, W. Li, X. Liu, S. Li, J. Yang, J. Hu, *J. Mater. Chem. A* **2014**, *2*, 16731; e) H. Chen, L. Hu, M. Chen, Y. Yan, L. Wu, *Adv. Funct. Mater.* **2014**, *24*, 934.
- [18] X. Wang, B. Liu, R. Liu, Q. Wang, X. Hou, D. Chen, R. Wang, G. Shen, *Angew. Chem. Int. Ed.* **2014**, *53*, 1849.
- [19] C. Debiemme-Chouvy, *Electrochem. Commun.* **2009**, *11*, 298.
- [20] S. Park, J. H. An, R. D. Piner, I. Jung, D. X. Yang, A. Velamakanni, S. T. Nguyen, R. S. Ruoff, *Chem. Mater.* **2008**, *20*, 6592.

Received: November 17, 2014

Revised: February 8, 2015

Published online: March 18, 2015